photonics

MDPI

Article

Temperature-Dependent Localized Surface Plasmon Resonances of Noble Nanoparticles Covered with Polymers

Dimitrios Ntemogiannis [1,*], Maria Tsarmpopoulou [1], Constantinos Moularas [2,†], Yiannis Deligiannakis [2], Alkeos Stamatelatos [1,‡], Dionysios M. Maratos [1], Nikolaos G. Ploumis [1], Vagelis Karoutsos [1], Spyridon Grammatikopoulos [1,3], Mihail Sigalas [1] and Panagiotis Poulopoulos [1,*]

[1] Department of Materials Science, University of Patras, 26504 Patras, Greece; mtsarmpopo@upatras.gr (M.T.); up1070376@upatras.gr (D.M.M.); up1053314@upnet.gr (N.G.P.); vkar@upatras.gr (V.K.); spiridongramma@upatras.gr (S.G.); sigalas@upatras.gr (M.S.)
[2] Laboratory of Physical Chemistry of Materials & Environment, Department of Physics, University of Ioannina, 45110 Ioannina, Greece; km1700@eohsi.rutgers.edu (C.M.); ideligia@uoi.gr (Y.D.)
[3] Department of Mechanical Engineering, University of Peloponnese, M. Alexandrou 1, 26334 Patras, Greece
* Correspondence: d.ntemogiannis@upnet.gr (D.N.); poulop@upatras.gr (P.P.); Tel.: +30-2610996383 (D.N.); +30-2610996388 (P.P.)
† Current address: Nanoscience and Advanced Materials Center (NAMC) EOHSI, Rutgers University, Piscataway, NJ 08854, USA.
‡ Current address: Department of Physics, University of Warwick, Coventry CV4 7AL, UK.

Abstract: Self-assembled gold and silver nanoparticles were fabricated in medium vacuum conditions on Corning glass substrates by means of DC magnetron sputtering. The samples were deposited either at 420 °C or 440 °C, or they were initially deposited at room temperature followed by post annealing. Subsequently, they were covered with three different polymers, namely Polystyrene-block-polybutadiene-blockpolystyrene (PS-b-PBD-b-PS), Polystyrene-co-methyl methacrylate (PS-co-PMMA) and Polystyreneblock-polyisoprene-block-polystyrene (PS-b-PI-b-PS), using spin coating. Localized surface plasmon resonances were recorded in the temperature range of −25 °C–100 °C. We show that the resonance position changes systematically as a function of temperature. Theoretical calculations carried out via the Rigorous Coupled Wave Analysis support the experimental results. Based on these findings, the investigated materials demonstrate potential as components for the development of temperature sensors.

Keywords: self-assembly; noble metal nanoparticles; plasmonics; temperature-dependent LSPRs; copolymers; hybrid nanostructured films; RCWA

check for updates

Citation: Ntemogiannis, D.; Tsarmpopoulou, M.; Moularas, C.; Deligiannakis, Y.; Stamatelatos, A.; Maratos, D.M.; Ploumis, N.G.; Karoutsos, V.; Grammatikopoulos, S.; Sigalas, M.; et al. Temperature-Dependent Localized Surface Plasmon Resonances of Noble Nanoparticles Covered with Polymers. *Photonics* **2024**, *11*, 618. https://doi.org/10.3390/photonics11070618

Received: 18 April 2024
Revised: 18 June 2024
Accepted: 27 June 2024
Published: 28 June 2024

Copyright: © 2024 by the authors. Licensee MDPI, Basel, Switzerland. This article is an open access article distributed under the terms and conditions of the Creative Commons Attribution (CC BY) license (https://creativecommons.org/licenses/by/4.0/).

1. Introduction

Localized surface plasmon resonance (LSPR) is a well-studied and highly intriguing phenomenon; it was observed in metal nanostructures, particularly nanoparticles (NPs). LSPRs manifest as collective oscillations of charge density on the surfaces of metallic nanoparticles upon irradiation via electromagnetic fields. When the frequency of incident light aligns with the plasma frequency of the free electrons within the nanoparticles, resonance occurs, resulting in the confinement of light and significant enhancement of the local electric field [1]. The plasmon resonance frequency and extinction intensity depend on the size, shape, size distribution, and composition of the nanostructures, as well as the refractive index of their surrounding dielectric environment [1–3].

The exploitation of LSPRs exhibited by plasmonic NPs has led to their widespread use across diverse fields including optoelectronics [4–6], solar cells [7,8], catalysis [9–11], biological and chemical sensing [12,13], bioimaging, photothermal therapy, drug delivery [8,14–16] and more [17]. Consequently, understanding the underlying mechanisms and phenomena governing the properties of these materials is of utmost importance.

Given the significance of the temperature dependence of LSPRs for a variety of applications, it is essential to comprehend how temperature changes can affect the optical properties and local dielectric environment around metallic nanoparticles, thereby influencing their LSPR characteristics. This effect can be harnessed in sensing applications, leveraging temperature-sensitive LSPRs for precise temperature monitoring [18–25]. In this context, various sensor configurations have been studied, among which the prism-based Kretschmann configuration has shown high sensitivity [19,23]. Furthermore, understanding LSPR temperature dependence is essential for ensuring the stability and reliability of plasmonic devices and optimizing the thermoplasmonic processes, which have implications in applications such as thermally assisted magnetic recording [26], catalysis [27], solar cells [28], photothermal therapy and other biological applications [29,30] among others [29,31]. Overall, studying the temperature effects on LSPRs can provide insights into the underlying physics, contributing to advancements in the development of functional devices and plasmonics research overall.

Several studies have delved into exploring the impact of temperature on the optical properties of various metallic materials, either in bulk [32,33], nanoparticle [3,34–39] or thin film form [40–46]. Moreover, research has been extended to other nanostructures [47,48] and alternative plasmonic materials like TiN [49]. These investigations have employed theoretical, experimental or combined approaches.

Focusing on the plasmon resonance in nanoparticles, previous studies have examined the temperature influence on the plasmon resonance absorption band in metal nanoparticles [50–53], as well as the origin of temperature effects on the surface plasmon resonance [54]. Furthermore, the size and temperature dependence of the surface plasmon resonance of colloidal gold NPs has been studied [34] at temperatures up to 72 °C. However, only a minor temperature effect was detected. It is worth noting that these studies were carried out a considerable time ago. The size and temperature effects on the surface plasmon resonance have also been investigated in spherical silver NPs embedded in a silica host matrix in the temperature range of 20–377 °C (293–650 K) [37]. Similarly, the temperature dependences of the surface plasmon resonance energy and width were studied for gold NPs in a silica host matrix in the temperature range 17–915 °C [3]. The same investigation has been also carried out for copper (Cu) NPs in the temperature range of 20–187 °C (293–460 K) [38]. The increase in temperature in the latter three studies led to appreciable red shift and broadening of the surface plasmon resonance in Au, Ag and Cu nanoparticles.

Another paper examined the temperature dependence of the surface plasmon resonance of Au NP dimers. A red shift and a band broadening of SPR were reported with an increase in temperature for all NP sizes. Additionally, a size-independent parameter was extracted, potentially useful in temperature sensing [35]. Moreover, an evaluation of the effects of temperature on the optical properties of phosphate glass containing Cu nanoparticles (NPs) and Cu^+ ions was carried out by means of optical absorption and photoluminescence (PL) spectroscopy measurements performed jointly in situ in the 25–300 °C (298 to 573 K) range. The surface plasmon resonance of Cu NPs showed a strong dampening effect with temperature [39]. Recently, the temperature dependence of Au/SiO_2 core–shell nanoparticles in water was investigated between room temperature and 80 °C. A decrease in absorption with temperature over the entire spectral range was observed, which was more pronounced at the LSPR position [36].

Based on the above, it is evident that despite the significant importance of the effect of temperature on the plasmon resonance for various applications and research areas, this topic has not received considerable attention until recently. Additionally, most of the cited studies have investigated optical properties such as the dielectric permittivity of the metals and other components involved in the proposed sensor configurations.

In contrast, this study focuses on the investigation of the temperature-dependent LSPR properties of a distinct type of hybrid nanocomposite films, consisting of self-assembled noble metal NPs covered with copolymers, through both experimental and theoretical approaches. These material systems possess unique properties that render them suitable for

diverse plasmonic applications [55]. Notably, the polymeric coatings provide structural integrity and protection from oxidation or other environmental factors, which is important for practical applications. Additionally, they can modify the dielectric environment of the NPs and consequently alter their LSPR response. The LSPR behavior of such systems has been previously examined at room temperature, showing remarkable tuning potential [55,56]. This study aims to further expand the understanding of the LSPR behavior of these distinct systems regarding their potential exploitation in temperature sensing applications. Moreover, it is important to note that the examined structures were fabricated via simple and cost-effective methods, highlighting their practicality and ease of implementation. LSPRs were recorded within the temperature range of −25–100 °C. This range was selected since it corresponds to typical environmental conditions and real-world scenarios where plasmonic systems are utilized.

More specifically, we studied the LSPR properties of self-assembled silver (Ag) and gold (Au) NPs located on glass substrates, both before and after coating with several copolymers across the temperature range of −25 to 100 °C. Expanding on the methods, Ag and Au self-assembled NPs were grown via magnetron sputtering either on heated Corning glass substrates or through post deposition annealing of Ag and Au thin films in air. Subsequently, three different copolymers were coated on top of the NPs by means of spin coating. The resonance position exhibited a systematic shift as a function of temperature, and the main contributions behind this effect are discussed. Furthermore, theoretical calculations carried out via the Rigorous Coupled Wave Analysis complement and support the experimental results. Finally, based on these results, we suggest that the investigated structures could be useful in the implementation of LSPR temperature sensor configurations.

2. Materials and Methods

2.1. Experimental Details

Self-assembled Ag and Au NPs were grown via direct-current (DC) magnetron sputtering on Corning glass substrates, either directly at 420 °C or 440 °C, or after post annealing of continuous thin films at 430 °C in air. A sputter-coater device (modified Balzers Union model SCD040, Oerlikon Balzers, Balzers, Liechtenstein) with a heated substrate holder was employed for the DC magnetron sputtering. During deposition at elevated temperatures, the substrate temperature was maintained constant via a temperature controller. By utilizing a dual-stage rotary pump, the base pressure of the chamber was maintained at 1.5×10^{-2} mbar. During deposition, argon was introduced into the chamber, increasing the total pressure to 5×10^{-2} mbar.

The term "films" is consistently used throughout the article to refer to each sample, along with their respective nominal thickness for identification purposes. Specifically, the term "films" refers to the nanostructured films which have been self-assembled into NPs, either directly or after post annealing. When we mention the nominal thickness of a nanostructured film deposited at 420 °C or 440 °C (directly self-assembled), we are referring to the thickness of a continuous film that would form under the same deposition time at room temperature. The direct formation of self-assembled nanoparticles on heated substrates occurs because gold and silver do not wet glass easily due to the large difference in their surface energies: 1.5 J/m^2 for Au, 1.25 J/m^2 for Ag [57] and only 0.3 J/m^2 for glass [58]. By elevating the temperature of the system, we drive it closer to the thermodynamic equilibrium state, which is island growth [59].

Following self-assembly, various copolymers were spin coated on the nanostructured films (noble metallic NPs). For the fabrication of the polymeric coatings (matrices), solid solutions of three different copolymers were used: polystyrene-block-polybutadiene-block-polystyrene (PS-b-PBD-b-PS), poly(styrene-co-methyl methacrylate) (PS-co-PMMA) and polystyrene-block-polyisoprene-block-polystyrene (PS-b-PI-b-PS), respectively. Each of the copolymers was dissolved in toluene to create a 1.5% w/w solution. Specifically, 0.092 g of PS-b-PBD-b-PS, 0.096 g of PS-co-PMMA and 0.065 g of PS-b-PI-b-PS were dissolved

in 6.143, 6.432 and 4.371 g of toluene solution, respectively. The copolymers were deposited on the films (NPs) using a Chemat Technology KW-4A spin-coating device (Chemat Technology, Northridge, CA, USA).

The surface morphology of the uncoated films was studied via atomic force microscopy (AFM). Film and polymer thickness determination was performed using AFM images showing the profile of a narrow scratch intentionally made on the film surface [56,60]. The thickness of polymer films deposited on a Corning glass substrate was measured at 54, 35 and 300 nm for PS-b-PBD-b-PS, PS-co-PMMA and PS-b-PI-b-PS, respectively. The employed AFM device was a Multimode Microscope with a Nanoscope IIIa controller and a 120 × 120 μm^2 magnet-free scanner (Model AS-130VMF) developed by Digital Instruments (Chapel Hill, NC, USA) operating in the non-contact (tapping) mode [61].

The optical properties of both polymer-coated and uncoated films were studied at room temperature via ultraviolet–visible (UV–Vis) spectroscopy using a Shimadzu UV-Vis spectrophotometer, Model: UV 1800 (Shimadzu, Kyoto, Japan) operating in the wavelength range of 200–1100 nm.

Temperature-Dependent UV–Vis Spectra

Regarding the temperature-dependent UV-Vis spectra, data were recorded using a Hitachi XX UV-Vis spectrophotometer (Hitachi, Tokyo, Japan) equipped with the temperature-control system, Unisoku cryostat (Unisoku, Osaka, Japan). The system allows temperature control within the range of ambient temperature up to 1000 °C using an N_2-heating stream [62]. The measured nanostructured films were placed into a quartz cuvette (3 × 1 × 1 cm), which was filled with an inert solvent to allow heat equilibrium between the nanoparticles–copolymer system and the liquid phase.

Two series of temperature-dependent measurements were carried out. The first series involved measurements of one Au film with a nominal thickness of 10 nm and two Ag films with nominal thicknesses of 6 and 10 nm, before and after coating. UV-Vis spectra were recorded in the −25 °C to 50 °C range with a step of 25 °C. In this series, ethanol was selected as an inert solvent and the polymeric coating used was PS-co-PMMA.

The second series involved measurements of three Au and three Ag polymer-coated nanostructured films. The nominal thickness of the Au specimens was 5 nm, while the Ag ones had nominal thicknesses of 5 and 10 nm as presented in Table 1. Measurements were carried out in the temperature range of 25–100 °C with a step of 25 °C. Xylene was used as a solvent; the measurements were very fast in order not to affect the polymers. In this case, three different polymeric coatings were used, PS-b-PBD-b-PS, PS-co-PMMA and PS-b-PI-b-PS. The films' stability was confirmed by remeasuring them after 3 days.

Table 1 summarizes the films deposited, their associated thermal processing and NP growth method, as well as their polymeric coatings to enhance the comprehension of the experimental procedure.

Table 1. List of all studied nanostructured films accompanied by their respective thermal processing–NP growth method and their polymeric coating.

Nanostructured Film (Nominal Thickness)	Thermal Processing-NP Growth Method	Polymeric Coating
First series		
Au1 (10 nm)	Post deposition annealing at 430 °C for 20′	PS-co-PMMA
Ag1 (6 nm)	Post deposition annealing at 430 °C for 8′	PS-co-PMMA
Ag2 (10 nm)	Post deposition annealing at 430 °C for 20′	PS-co-PMMA

Table 1. *Cont.*

Nanostructured Film (Nominal Thickness)	Thermal Processing-NP Growth Method	Polymeric Coating
Second series		
Au2 (5 nm)	Direct self-assembly (deposition at 440 °C) [56]	PS-b-PBD-b-PS
Au3 (5 nm)	Direct self-assembly (deposition at 440 °C) [56]	PS-co-PMMA
Au4 (5 nm)	Direct self-assembly (deposition at 440 °C) [56]	PS-b-PI-b-PS
Ag3 (5 nm)	Direct self-assembly (deposition at 420 °C) [55]	PS-b-PBD-b-PS
Ag4 (5 nm)	Direct self-assembly (deposition at 420 °C) [55]	PS-co-PMMA
Ag5 (10 nm)	Direct self-assembly (deposition at 420 °C) [55]	PS-b-PI-b-PS

2.2. Theoretical Model

The system under examination is depicted in Figure 1. NPs are represented as cubes and cylinders as they facilitate accelerated computational processing when implementing the RCWA method [56,60,63]. The NPs were situated on a SiO_2 substrate, surrounded by a polymeric matrix. For net Ag or Au NPs, the polymeric matrix was replaced with air. Furthermore, when simulating the temperature-dependent measurements, an inert solvent was located on top of the polymeric matrix.

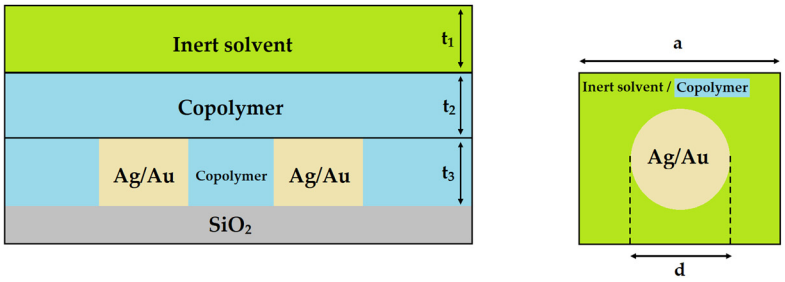


Figure 1. The examined system of Ag or Au NPs on glass substrate surrounded by copolymers. For temperature-dependent simulations, an inert solvent was applied onto the copolymer. Side view (**left**) and top view (**right**). "a" is the lattice constant, "d" the diameter of the NPs, "t_3" their height, while "t_1" and "t_2"denote the thickness of the inert solvent and copolymer, respectively.

Previous articles [63,64] have demonstrated that despite the non-periodical behavior of materials fabricated through experimental methods, there is an alignment between the theoretical and experimental results. Calculating the experimentally fabricated disordered structure is very challenging, if not impossible, as it requires computations within an extensive supercell, demanding significant time and memory resources. On the other hand, relying solely on the calculation of individual metal nanoparticles proves unreliable, as the experimental findings indicate that nanoparticles are typically positioned near one another. Hence, a periodic array between nanoparticles was employed. The Rigorous Coupled-Wave Analysis (RCWA) method stands out as a crucial tool characterized by the accuracy of its results when analyzing propagating electromagnetic waves within periodic matrices [65]. Additionally, RCWA offers computational efficiency by dividing the analyzed area into layers with consistent refractive index values. More details on the theoretical model used can be found in previous studies [55,56,60,63,64].

3. Results

The Section 3 is divided into two subsections. The first subsection includes AFM images depicting the surface morphology of the self-assembled NPs grown after post deposition annealing, along with their respective NP size distributions. Furthermore, UV-Vis spectra of the post annealed films, both uncoated and coated with PS-co-PMMA, are also presented. In the second subsection, the temperature-dependent LSPRs of self-assembled NPs grown on heated substrates are presented. These samples were coated with various copolymers. Their LSPRs and microstructure have been discussed in detail in references [55,56].

3.1. Microstructure and LSPRs at Room Temperature

Figure 2a,c show the surface morphology of two Ag nanostructured films with nominal thicknesses of 6 and 10 nm, respectively (Ag1 and Ag2), while Figure 3a shows the surface morphology of a 10 nm Au film (Au1). Figure 2b,d and Figure 3b illustrate the corresponding NP size distributions. All the films were self-assembled into NPs after post deposition annealing at 430 °C.

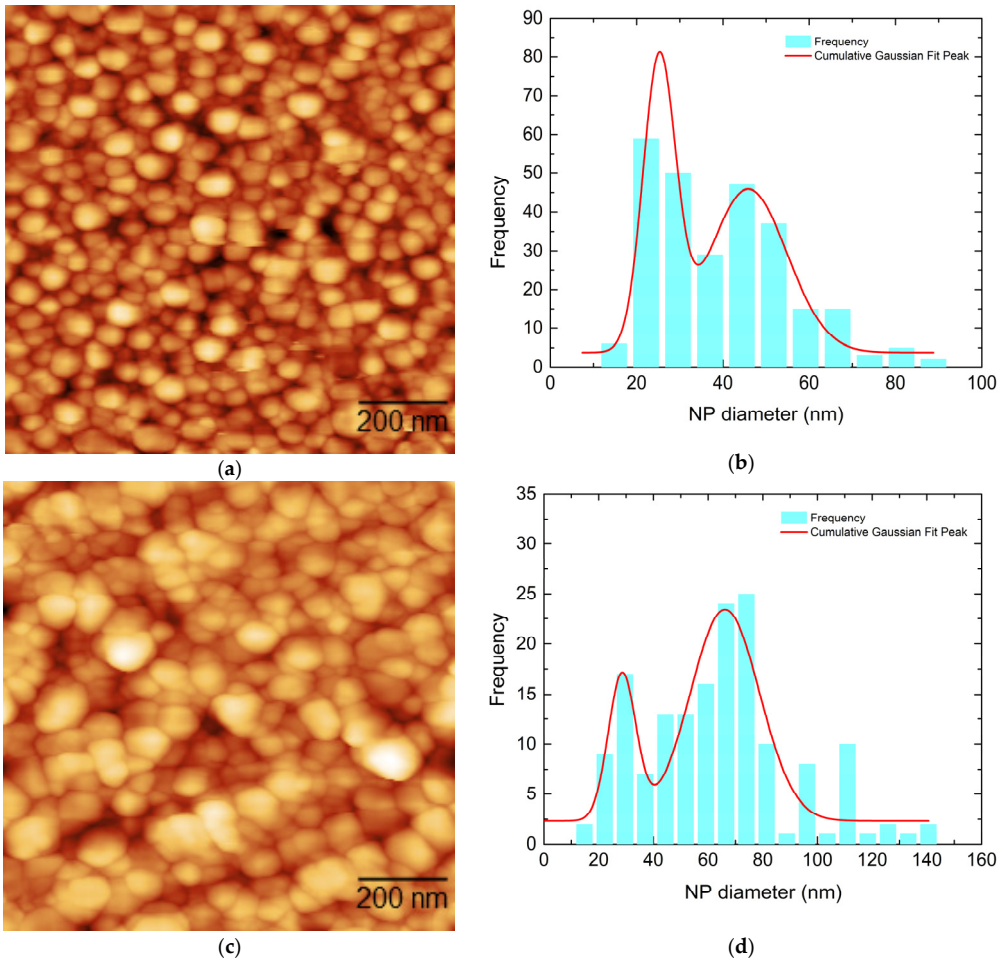
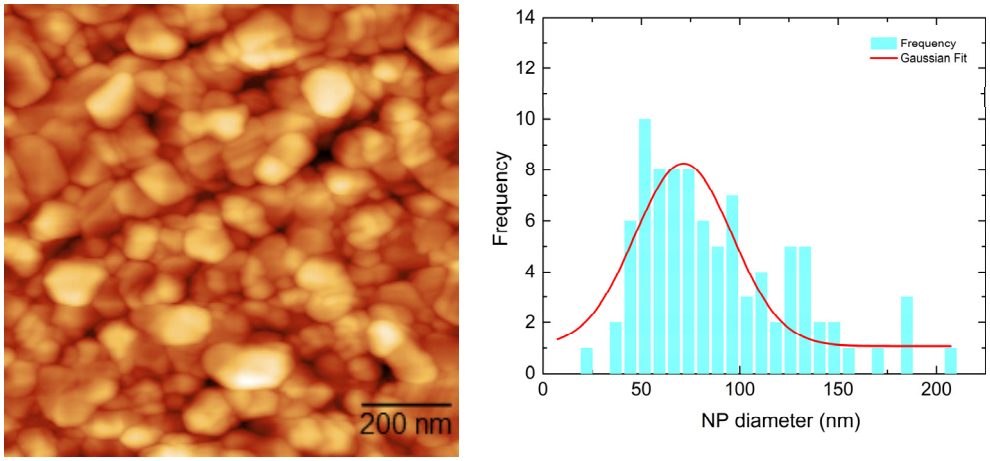


Figure 2. (**a**,**c**) AFM images of the nanostructured Ag films deposited at 420 °C along with their respective nanoparticle diameter distributions (**b**,**d**). (**a**,**b**) correspond to Ag1 (6 nm), and (**c**,**d**) correspond to Ag2 (10 nm).

Dense NP distributions with several agglomerates could be observed for all cases. For the Ag nanostructured films, bimodal distributions of NPs were observed in both cases, with the initially thicker film (Ag2—10 nm) showing larger NPs on average, as revealed by their NP size distributions (Figure 2b,d). The fitting was performed using the Gaussian

distribution function. The detailed average NP diameter values are presented in Table 2. On the other hand, for the Au nanostructured film, a single broad NP distribution was observed, with some agglomerates also present.



(a) **(b)**

Figure 3. (**a**) AFM image of the nanostructured Au1 film (10 nm) deposited at 440 °C along with its respective nanoparticle diameter distribution (**b**).

Table 2. Mean NP diameter values for NP distributions shown in Figure 2b,d and Figure 3b.

Nanostructured Film	Mean NP Diameter	
Ag1 (6 nm)	25 nm	46 nm
Ag2 (10 nm)	29 nm	66 nm
Au1 (10 nm)	72 nm	

Figure 4a,b show the UV-Vis spectra recorded at room temperature for the aforementioned nanostructured films before and after covering them with PS-co-PMMA. Figure 4a corresponds to the Ag specimens, depicting absorbance curves with a main resonance peak around 450 nm and a secondary one around 355 nm. This observation can be attributed to the bimodal growth of the NPs. Furthermore, the LSPR amplitude of the initially thicker (10 nm) film was greater than the thinner one. This was expected, due to the larger size of the NPs observed in the former case. Regarding the nanoparticles with diameters beyond 10 nm, larger NPs were expected to exhibit LSPRs at longer wavelengths (red-shift) [59,66–68]. However, this was not observed in our Ag samples due to their bimodal size distributions and non-perfectly spherical shapes. After coating with PS-co-PMMA, a red shift was observed for both cases, along with an increase in the LSPR amplitude. These phenomena were more pronounced for the thinner film. Furthermore, the width of the resonance slightly increased in both cases after coating with the copolymer. These observations could be attributed to the higher dielectric constant of the polymeric coatings (~1.5) compared to that of air. The same trend was also observed when examining the influence of the same polymeric coatings on the plasmonic behavior of Au and Ag NPs [55,56]. Additionally, a consistent red shift was also observed in the Au and Ag NPs in NiO [63,69] and ZnO [60] dielectric environments, due to their relatively large dielectric constants.

Figure 4b corresponds to the Au specimen, displaying a single-peak broad resonance, consistent with the observed broad single distribution of Figure 3b. For the uncoated specimen, the LSPR is located at 582 nm. After covering with PS-co-PMMA, a red shift was observed once again, accompanied by an increase in the LSPR amplitude and a slight broadening of the resonance. This phenomenon could be attributed to the larger dielectric constant of the polymeric coating compared to that of air [55,56].

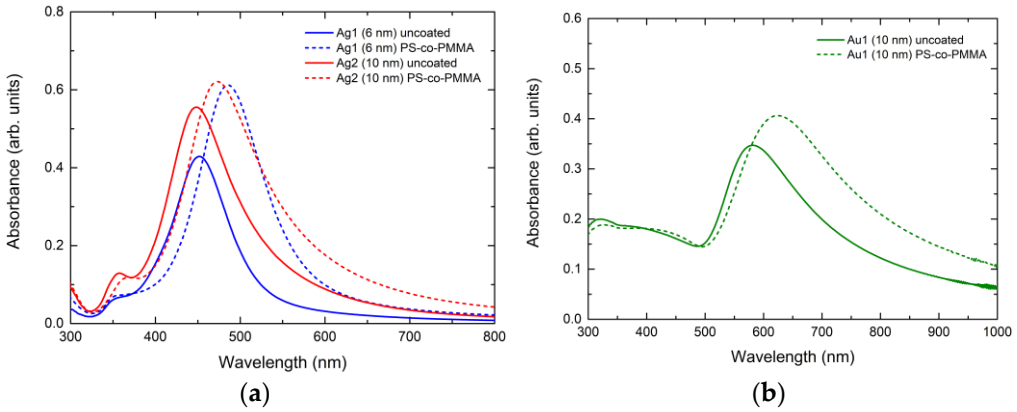


Figure 4. (**a**) UV-Vis spectra for the two nanostructured Ag films (Ag1 and Ag2) with nominal thicknesses of 6 and 10 nm, respectively. (**b**) UV-Vis spectra for the nanostructured Au film (Au1) with a nominal thickness of 10 nm. Solid lines show absorbance curves before coating and dashed lines depict those following the coating with PS-co-PMMA.

3.2. Temperature-Dependent LSPRs

In Figure 5, we present the temperature-dependent absorbance for polymer-coated Ag and Au NPs on Corning glass, as indicated. Due to the setup specifications, the samples had to be embedded in cubes filled with an inert solvent in order to ensure homogeneous heating. However, this resulted in increased noise. In order to minimize the error in the determination of the LSPR position we performed the work as follows: For Ag spectra, where no background appears, before determination of the LSPR position we performed either some soft smooth (adjusting average), like in Figure 5a,b, or we fitted the resonance with a Gaussian. The difference between the two methods is very small. It has to be noted that the measurements had an error margin of ± 0.5 nm regarding the wavelength of the LSPR position. Figure 5a,b show an unambiguous blue shift of the LSPR position with increasing temperature. For the Au spectra, which show some slope, see Figure 5c; we followed the process presented in Ref. [70], i.e., correction for the background and Gaussian fitting; see Figure 5d. Even for this sample in which the blue shift is among the smallest observed, the shift is unambiguous.

In Figure 6, we present the change $\Delta\lambda$ in the position of the LSPR with increasing temperature for the polymer-covered Ag and Au NPs on Corning glass. We define $\Delta\lambda$ as the difference between the wavelength of the LSPR position of a sample at a specific temperature minus the one at the lowest temperature for each set of measurements. The negative slope reveals that by increasing the temperature, the LSPR position moves to a smaller wavelength, i.e., a "blue shift" is always observed. We will next discuss these data with respect to theoretical calculation via the RCWA method and the existing literature in the Section 4.

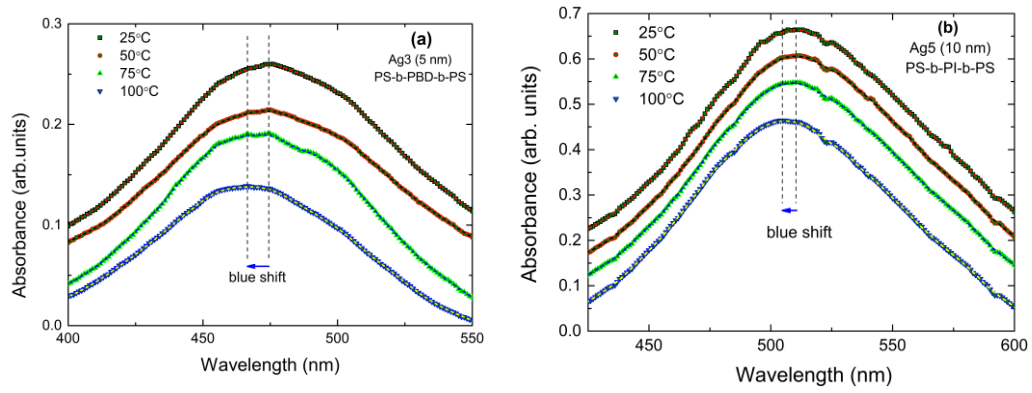


Figure 5. *Cont.*

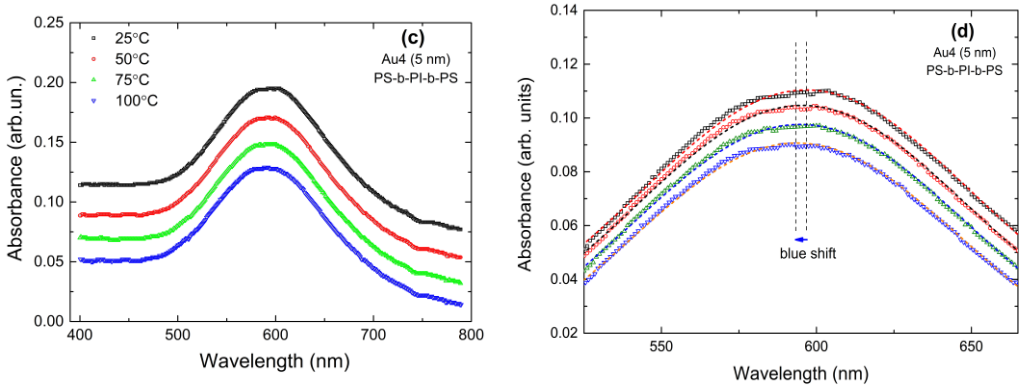


Figure 5. Temperature-dependent LSPRs in polymer-coated Ag and Au NPs. The dashed lines are fitted curves. We zoomed the spectra so that the blue shift is clearly visible. (**a**) corresponds to Ag3 (5 nm) covered with PS-b-PBD-b-PS, (**b**) corresponds to Ag5 (10 nm) covered with PS-b-PI-b-PS, and (**c**) corresponds to Au4 (5 nm) covered with PS-b-PI-b-PS. (**d**) shows the absorbance curves of Au4 (5 nm) after correcting the background and performing Gaussian fitting.

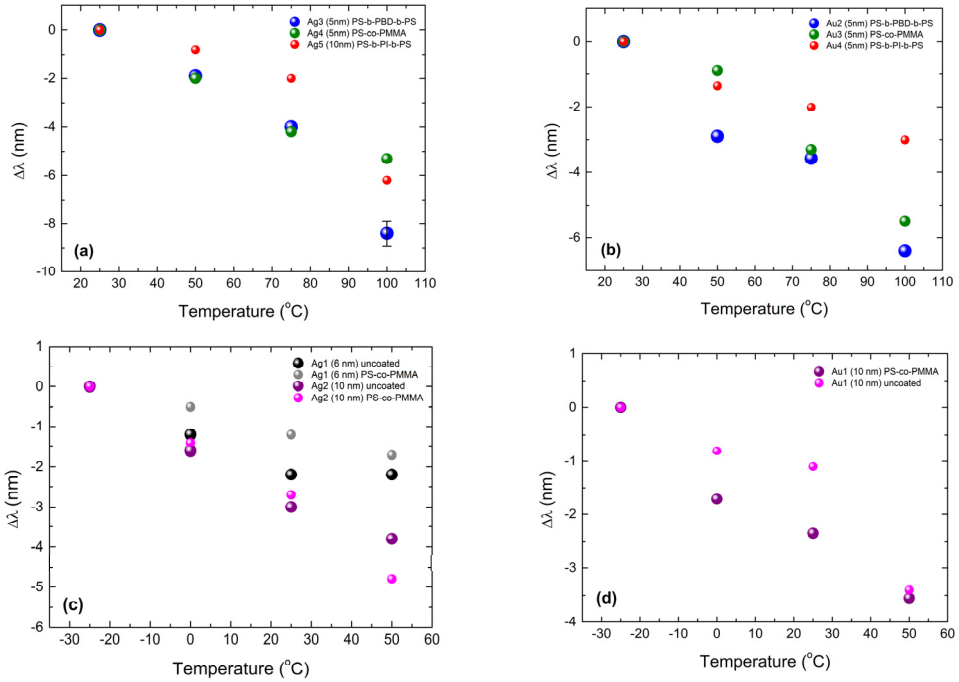


Figure 6. Change in the LSPR position as a function of temperature for polymer-covered Ag and Au NPs on Corning glass. (**a**) shows the temperature-dependent LSPR position change of Ag specimens: Ag3 (5 nm), Ag4 (5 nm) and Ag5 (10 nm) covered with PS-b-PBD-b-PS, PS-co-PMMA and PS-b-PI-b-PS respectively. (**b**) shows the same as (**a**) but for Au specimens: Au2 (5 nm), Au3 (5 nm), Au4 (5 nm) also covered with PS-b-PBD-b-PS, PS-co-PMMA and PS-b-PI-b-PS respectively. (**c**) shows the temperature-dependent LSPR position change of Ag1 (6 nm) and Ag2 (10 nm) before and after covering with PS-co-PMMA. (**d**) shows the same as (**c**), but for the Au1 (10 nm) specimen.

4. Discussion

In this section, the theoretical calculations conducted via the RCWA method are presented to complement the experimental results.

In Refs [3,37,38], Yeschenko et al. studied the temperature dependence of LSPRs of gold, silver and copper NPs embedded in glass. They found a red shift of the LSPRs with increasing temperature. This means that the resonance position decreases in terms of energy in eV (or, equivalently, increases in terms of wavelength in nm) as the temperature

increases. Three main factors govern the appearance of the red shift. One very small contribution is due to the increase of the refractive index of glass in the temperature interval of the studies. As this change is tiny (in the fourth decimal place) this contribution is almost negligible. A slightly bigger change is due to the fundamental temperature dependence of the electron–phonon scattering. A third, major contribution comes from the free three-dimensional expansion of the metallic nanoparticles with increasing temperature. For example, for copper, for a temperature increase of between 27 and 177 °C (300–450 K) the total red shift was about 9 meV (less than 3 nm in wavelength) [38]. For the Ag NPs, the effect seemed to be about three times larger [37].

On the contrary, in our samples, the LSPRs showed a clear blue shift with increasing temperature. Employing our ability to perform rigorous calculations with the help of the RCWA method, we provide below three quite important sources of blue shift for the LSPRs of our NPs coated with polymers. As a case study, we selected Ag NPs with a mean diameter d of 30 nm, such as some of our experimental ones; see Table 2. We selected a = 3/2 × d and t_3 = d/3 as in [55]. We selected PS-co-PMMA as a cover with a thickness t_2 = 35 nm.

First, we discuss the effect of a decrease in the refractive index of the polymer coating with increasing temperature. We followed this approach as the PS-co-PMMA refractive index indeed decreased linearly with temperature in the temperature interval of our measurements [71]. The rate of decrease was about a 0.01 per 100 °C increase in temperature [71]. Although it is not very large, it is one order of magnitude larger than the increase in the glass refractive index in the same temperature interval [72]. Therefore, we ignored the influence of the increase in the refractive index of our glass substrate, which would have given a very small red shift contribution as in Refs. [3,37,38].

In Figure 7, one can see the calculated absorbance spectra of our system when keeping all the parameters constant and decreasing the polymer refractive index by an initial value n = 1.49 and a step of about 2%. A clear blue shift of the LSPRs is demonstrated. In the inset, we present the quantity Δλ (blue shift) as a function of minus n. We selected minus n as the X-axis for the inset to look like the experimental data of Figure 6. As the experimental increase in temperature by 75 °C corresponded to a decrease in n of PS-co-PMMA by only 0.0075 [71], from the inset of Figure 7, we estimated that this effect resulted in a decrease in the wavelength of the LSPR position by Δλ~−1.5 nm.

Second, we discuss the effect of a decrease in the refractive index n of the liquid surrounding our samples, during the temperature-dependent measurements, with increasing temperature. In Figure 8, we present the absorbance spectra of our system when keeping all the parameters constant and this time, decreased the ethanol refractive index by an initial value n = 1.36 and a step of about 2%. We took an indicative ethanol layer thickness of 500 nm, i.e., much larger than the thickness of PS-co-PMMA, to represent the case of infinite as the ethanol layer around the sample was found at the macroscopic scale. Here, we just aim to demonstrate the effects without increasing enormously the computational time. A clear blue shift of the LSPRs is demonstrated in Figure 8. In the inset, we present the quantity Δλ as a function of the decrease in $-n$ of ethanol. The slope of this line is about 20% smaller than the one in the inset of Figure 7. This seems to be reasonable as PS-co-PMMA directly covered the NPs while ethanol did not. However, ethanol exhibits a much stronger temperature decrease in its refractive index with increasing temperature as compared to PS-co-PMMA [73]. For example, the rate of linear decrease in the n of ethanol was 0.04 per 100 °C as the temperature increased between 0 and 25 °C [73]. Then, the value of the blue shift which corresponded to a decrease in n by 0.03 (i.e., the one corresponding to the experimental increase in temperature by 75 °C; see Figure 6) was Δλ~−4.2 nm. Since the refractive index of xylene has a slightly stronger temperature dependence than that of ethanol [74], the effect of xylene on the Δλ of the LSPRs of our NPs was expected also to be slightly larger than that of ethanol. Finally, with this analysis in mind, we can also understand why the NPs covered with the very thick polymeric layers (case of PS-b-PI-b-PS) showed less strong temperature-dependent LSPRs compared to the other ones (PS-co-PMMA, PS-b-PBD-b-PS)(see Figure 6a,b): the very thick PS-b-PI-b-PS

polymer layers shield the strong effects of the surrounding liquid upon the change in the LSPRs position.

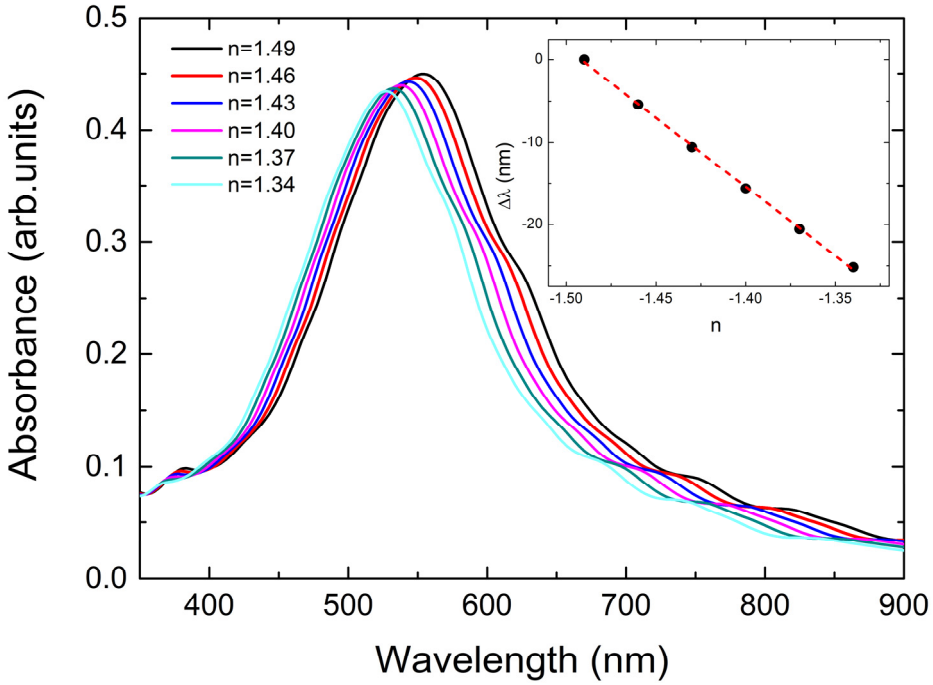


Figure 7. Change in the LSPR position as a function of the refractive index of PS-co-PMMA. A clear blue shift is observed. In the inset, we plot the blue shift as a function of $-n$. The dashed line is the result of linear fitting.

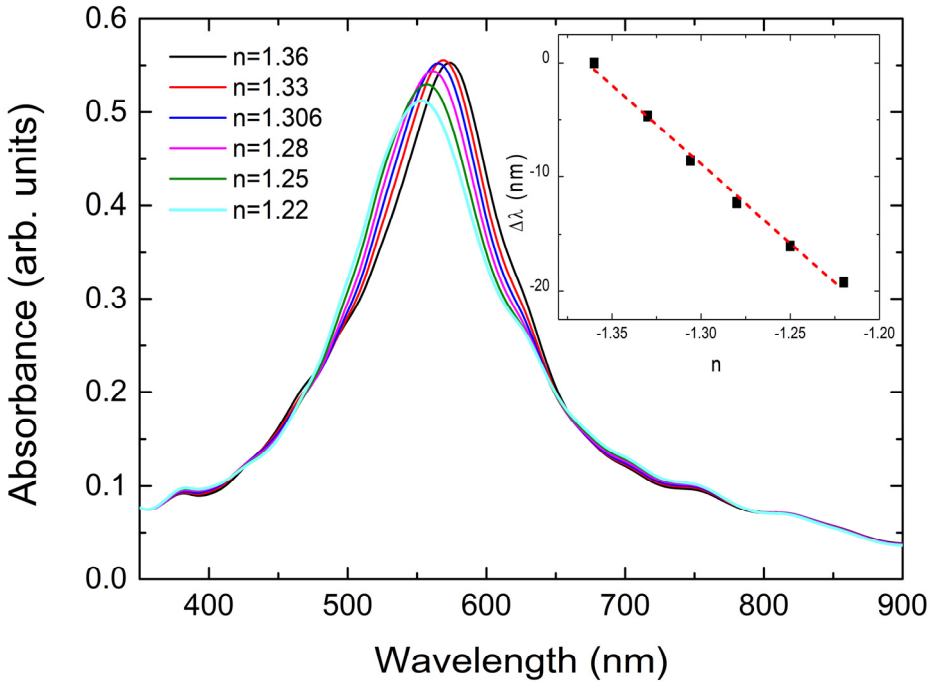


Figure 8. Change in the LSPR position as a function of the refractive index of ethanol. A clear blue shift is observed. In the inset, we plot the blue shift as a function of $-n$. The dashed line is the result of linear fitting.

The aforementioned decrease in the n of the polymer or the liquid around the samples during the measurements had a quite significant contribution to the blue shift of the LSPRs.

Here, we will discuss a third, relatively small contribution originating from the selective expansion of our NPs. In [3,37,38], the NPs were placed inside self-assembled cavities in the glass matrix, and they were free to fully expand in all directions during heating. In our case, the NPs were bounded on glass. The linear expansion coefficient α of silver, for example, is orders of magnitude larger than that of glass and reaches a value of about 0.002 per temperature increase of 100 °C. As silver NPs cannot expand on the film plane due to their attachment to the glass, they can expand only along the normal in the glass plane direction. Then, there are two options. Either the NPs' height increases by only 0.2% along the normal to the substrate plane, or, if the total volume has to remain constant to minimize the elastic energy of the system, the NPs should by elongated in the Z direction (normal of the film plane) by about 0.6% to accommodate the actual contraction along the X and Y axes on the film plane, similar to the strained epitaxy of metallic thin films; see, e.g., [75]. In the latter case, we plot in Figure 9 the absorbance spectra of our system whilst keeping all the parameters constant as in Figure 7 for $n = 1.49$ and increasing t_3 (NPs height) by an initial value $t_3 = 10$ nm and a step of 2%. The blue shift corresponding to an increase of 75 °C is only $\Delta\lambda = -0.7$ nm.

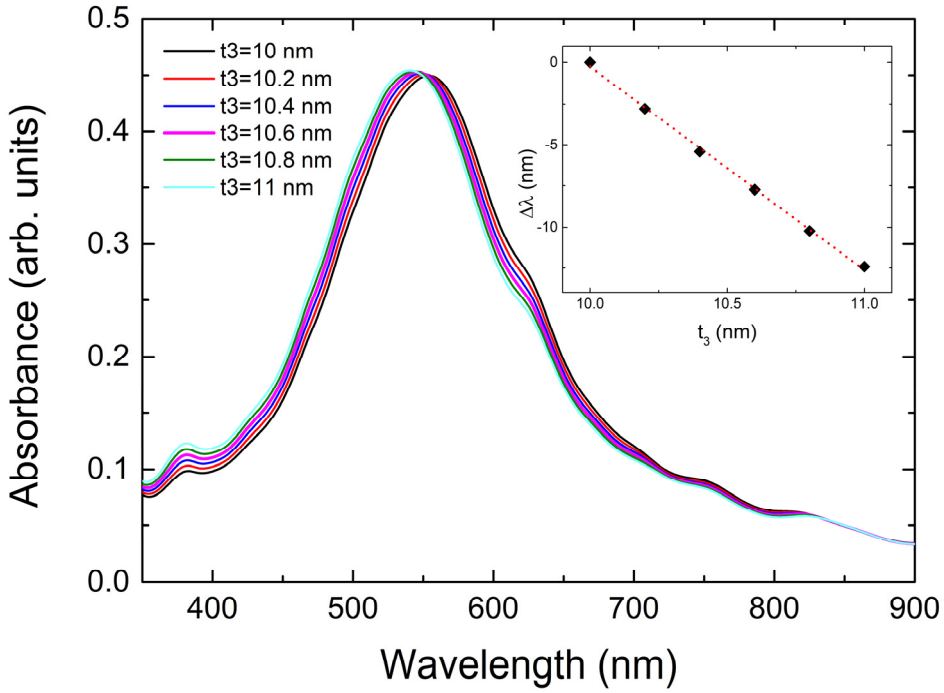


Figure 9. Change in the LSPR position as a function of the height t_3 of the NPs. A clear blue shift is observed. In the inset, we plot the blue shift as a function of t_3. The dashed line is the result of linear fitting.

Adding all three contributions, one may expect a total blue shift of about $\Delta\lambda = -6.5$ nm for a temperature increase of 75 °C. This is in fair agreement with the experimental data of Figure 6. We have to notice that our calculations have shown that another blue shift contribution may arise when the medium is elastic and allows for the distance between the particles to increase with the temperature. Although this contribution is important, it is not encountered in the experimental NPs of this work, and it can be discussed in a forthcoming publication.

Finally, although the change of the LSPRs' position with increasing temperature was not as large as that of SPRs in other works of literature Ref. [24], the linear dependence of all the contributions that we studied via experiment and theory make the systems under investigation appealing for potential use in the fabrication of temperature sensors.

5. Conclusions

In summary, the main target of this work was to study the temperature dependence of the position of the maximum intensity, i.e., the LSPR position of the absorbance of the silver and gold NPs self-assembled on Corning glass and then covered with polymeric coatings. We found a linear decrease in the LSPR position in wavelength units as the temperature increases. With the help of rigorous calculations via the RCWA method, we disentangled this "blue shift" of the LSPRs into three contributions: the temperature-dependent decrease in the refractive index of the polymeric coating and of the liquid necessary to embed the films for homogeneous and fast heating and the increase in the NPs' height. The linear dependence of these contributions on temperature may guarantee the fabrication of a temperature sensor.

Author Contributions: Conceptualization, M.S.; methodology, P.P. and Y.D.; software, M.T. and D.N.; validation, P.P., M.S. and Y.D.; formal analysis, C.M.; investigation, C.M., A.S., N.G.P., D.M.M. and V.K.; resources, Y.D., M.S. and P.P.; data curation, C.M. and P.P.; writing—original draft preparation, D.N. and P.P.; writing—review and editing, S.G., M.S. and Y.D.; visualization, S.G. and M.S.; supervision, M.S. and S.G.; project administration, P.P., M.S. and Y.D. All authors have read and agreed to the published version of the manuscript.

Funding: This research received no external funding.

Institutional Review Board Statement: Not applicable.

Informed Consent Statement: Not applicable.

Data Availability Statement: Data are contained within the article.

Conflicts of Interest: The authors declare no conflicts of interest.

References

1. Hutter, E.; Fendler, J.H. Exploitation of Localized Surface Plasmon Resonance. *Adv. Mater.* **2004**, *16*, 1685–1706. [CrossRef]
2. Mayer, K.M.; Hafner, J.H. Localized Surface Plasmon Resonance Sensors. *Chem. Rev.* **2011**, *111*, 3828–3857. [CrossRef] [PubMed]
3. Yeshchenko, O.A.; Bondarchuk, I.S.; Gurin, V.S.; Dmitruk, I.M.; Kotko, A.V. Temperature Dependence of the Surface Plasmon Resonance in Gold Nanoparticles. *Surf. Sci.* **2013**, *608*, 275–281. [CrossRef]
4. Kunwar, S.; Pandit, S.; Jeong, J.-H.; Lee, J. Improved Photoresponse of UV Photodetectors by the Incorporation of Plasmonic Nanoparticles on GaN through the Resonant Coupling of Localized Surface Plasmon Resonance. *Nano-Micro Lett.* **2020**, *12*, 91. [CrossRef] [PubMed]
5. Liang, Z.; Sun, J.; Jiang, Y.; Jiang, L.; Chen, X. Plasmonic Enhanced Optoelectronic Devices. *Plasmonics* **2014**, *9*, 859–866. [CrossRef]
6. Xu, L.; Miao, J.; Chen, Y.; Su, J.; Yang, M.; Zhang, L.; Zhao, L.; Ding, S. Characterization of Ag-Doped ZnO Thin Film for Its Potential Applications in Optoelectronic Devices. *Optik* **2018**, *170*, 484–491. [CrossRef]
7. Atwater, H.A.; Polman, A. Plasmonics for Improved Photovoltaic Devices. *Nat. Mater.* **2010**, *9*, 205–213. [CrossRef] [PubMed]
8. De Aberasturi, D.J.; Serrano-Montes, A.B.; Liz-Marzán, L.M. Modern Applications of Plasmonic Nanoparticles: From Energy to Health. *Adv. Opt. Mater.* **2015**, *3*, 602–617. [CrossRef]
9. Da Silva, A.G.M.; Rodrigues, T.S.; Wang, J.; Camargo, P.H.C. Plasmonic Catalysis with Designer Nanoparticles. *Chem. Commun.* **2022**, *58*, 2055–2074. [CrossRef]
10. Li, S.; Miao, P.; Zhang, Y.; Wu, J.; Zhang, B.; Du, Y.; Han, X.; Sun, J.; Xu, P. Recent Advances in Plasmonic Nanostructures for Enhanced Photocatalysis and Electrocatalysis. *Adv. Mater.* **2021**, *33*, 2000086. [CrossRef]
11. Nie, M.; Liao, J.; Cai, H.; Sun, H.; Xue, Z.; Guo, P.; Wu, M. Photocatalytic Property of Silver Enhanced Ag/ZnO Composite Catalyst. *Chem. Phys. Lett.* **2021**, *768*, 138394. [CrossRef]
12. Zeng, S.; Baillargeat, D.; Ho, H.-P.; Yong, K.-T. Nanomaterials Enhanced Surface Plasmon Resonance for Biological and Chemical Sensing Applications. *Chem. Soc. Rev.* **2014**, *43*, 3426. [CrossRef]
13. Demishkevich, E.; Zyubin, A.; Seteikin, A.; Samusev, I.; Park, I.; Hwangbo, C.K.; Choi, E.H.; Lee, G.J. Synthesis Methods and Optical Sensing Applications of Plasmonic Metal Nanoparticles Made from Rhodium, Platinum, Gold, or Silver. *Materials* **2023**, *16*, 3342. [CrossRef]
14. Sharifi, M.; Attar, F.; Saboury, A.A.; Akhtari, K.; Hooshmand, N.; Hasan, A.; El-Sayed, M.A.; Falahati, M. Plasmonic Gold Nanoparticles: Optical Manipulation, Imaging, Drug Delivery and Therapy. *J. Control. Release* **2019**, *311–312*, 170–189. [CrossRef]
15. Austin, L.A.; Mackey, M.A.; Dreaden, E.C.; El-Sayed, M.A. The Optical, Photothermal, and Facile Surface Chemical Properties of Gold and Silver Nanoparticles in Biodiagnostics, Therapy, and Drug Delivery. *Arch. Toxicol.* **2014**, *88*, 1391–1417. [CrossRef]
16. Kim, M.; Lee, J.; Nam, J. Plasmonic Photothermal Nanoparticles for Biomedical Applications. *Adv. Sci.* **2019**, *6*, 1900471. [CrossRef]

17. Liu, J.; He, H.; Xiao, D.; Yin, S.; Ji, W.; Jiang, S.; Luo, D.; Wang, B.; Liu, Y. Recent Advances of Plasmonic Nanoparticles and Their Applications. *Materials* **2018**, *11*, 1833. [CrossRef]
18. Chiang, H.-P.; Wang, Y.-C.; Leung, P.T.; Tse, W.S. A Theoretical Model for the Temperature-Dependent Sensitivity of the Optical Sensor Based on Surface Plasmon Resonance. *Opt. Commun.* **2001**, *188*, 283–289. [CrossRef]
19. Ozdemir, S.K.; Turhan-Sayan, G. Temperature Effects on Surface Plasmon Resonance: Design Considerations for an Optical Temperature Sensor. *J. Light. Technol.* **2003**, *21*, 805–814. [CrossRef]
20. Peng, Y.; Hou, J.; Huang, Z.; Lu, Q. Temperature Sensor Based on Surface Plasmon Resonance within Selectively Coated Photonic Crystal Fiber. *Appl. Opt.* **2012**, *51*, 6361. [CrossRef] [PubMed]
21. Velázquez-González, J.S.; Monzón-Hernández, D.; Moreno-Hernández, D.; Martínez-Piñón, F.; Hernández-Romano, I. Simultaneous Measurement of Refractive Index and Temperature Using a SPR-Based Fiber Optic Sensor. *Sens. Actuators B Chem.* **2017**, *242*, 912–920. [CrossRef]
22. Ibrahim, J.; Al Masri, M.; Verrier, I.; Kampfe, T.; Veillas, C.; Celle, F.; Cioulachtjian, S.; Lefèvre, F.; Jourlin, Y. Surface Plasmon Resonance Based Temperature Sensors in Liquid Environment. *Sensors* **2019**, *19*, 3354. [CrossRef] [PubMed]
23. Yu, H.; Sun, X.; Liu, G.; Fateh, U.; Ban, D.; Deng, N.; Qiu, F. Gas Environment Independent Temperature Sensor via Double-Metal Surface Plasmon Resonance. *Opt. Express* **2021**, *29*, 15393. [CrossRef]
24. Song, Y.; Sun, M.; Wu, H.; Zhao, W.; Wang, Q. Temperature Sensor Based on Surface Plasmon Resonance with TiO_2-Au-TiO_2 Triple Structure. *Materials* **2022**, *15*, 7766. [CrossRef]
25. Zhang, X.; Xu, Y.; Zhu, X.-S.; Shi, Y.-W. Surface Plasmon Resonance Temperature Sensor with Tunable Detection Range Based on a Silver-Coated Multi-Hole Optical Fiber. *Opt. Express* **2022**, *30*, 48091. [CrossRef] [PubMed]
26. Zhou, N.; Xu, X.; Hammack, A.T.; Stipe, B.C.; Gao, K.; Scholz, W.; Gage, E.C. Plasmonic Near-Field Transducer for Heat-Assisted Magnetic Recording. *Nanophotonics* **2014**, *3*, 141–155. [CrossRef]
27. Moularas, C.; Gemenetzi, A.; Deligiannakis, Y.; Louloudi, M. Nanoplasmonics in Catalysis for Energy Technologies: The Concept of Plasmon-Assisted Molecular Catalysis (PAMC). *Nanoenergy Adv.* **2023**, *4*, 25–44. [CrossRef]
28. Liu, G.; Xu, J.; Chen, T.; Wang, K. Progress in Thermoplasmonics for Solar Energy Applications. *Phys. Rep.* **2022**, *981*, 1–50. [CrossRef]
29. Baffou, G.; Cichos, F.; Quidant, R. Applications and Challenges of Thermoplasmonics. *Nat. Mater.* **2020**, *19*, 946–958. [CrossRef]
30. Ruhoff, V.T.; Arastoo, M.R.; Moreno-Pescador, G.; Bendix, P.M. Biological Applications of Thermoplasmonics. *Nano Lett.* **2024**, *24*, 777–789. [CrossRef]
31. Lin, K.-T.; Lin, H.; Jia, B. Plasmonic Nanostructures in Photodetection, Energy Conversion and Beyond. *Nanophotonics* **2020**, *9*, 3135–3163. [CrossRef]
32. Winsemius, P.; Kampen, F.F.V.; Lengkeek, H.P.; Went, C.G.V. Temperature Dependence of the Optical Properties of Au, Ag and Cu. *J. Phys. F Met. Phys.* **1976**, *6*, 1583–1606. [CrossRef]
33. Liljenvall, H.G.; Mathewson, A.G. The Optical Properties of Silver in the Energy Range 3.2–4.3 eV as a Function of Temperature. *J. Phys. C Solid State Phys.* **1970**, *3*, S341–S347. [CrossRef]
34. Link, S.; El-Sayed, M.A. Size and Temperature Dependence of the Plasmon Absorption of Colloidal Gold Nanoparticles. *J. Phys. Chem. B* **1999**, *103*, 4212–4217. [CrossRef]
35. Maurya, M.R.; Toutam, V. Size-Independent Parameter for Temperature-Dependent Surface Plasmon Resonance in Metal Nanoparticles. *J. Phys. Chem. C* **2016**, *120*, 19316–19321. [CrossRef]
36. Wang, L.; Zare, D.; Chow, T.H.; Wang, J.; Magnozzi, M.; Chergui, M. Disentangling Light- and Temperature-Induced Thermal Effects in Colloidal Au Nanoparticles. *J. Phys. Chem. C* **2022**, *126*, 3591–3599. [CrossRef] [PubMed]
37. Yeshchenko, O.A.; Dmitruk, I.M.; Alexeenko, A.A.; Kotko, A.V.; Verdal, J.; Pinchuk, A.O. Size and Temperature Effects on the Surface Plasmon Resonance in Silver Nanoparticles. *Plasmonics* **2012**, *7*, 685–694. [CrossRef]
38. Yeshchenko, O.A. Temperature Effects on the Surface Plasmon Resonance in Copper Nanoparticles. *Ukr. J. Phys.* **2013**, *58*, 249–259. [CrossRef]
39. Jiménez, J.A. Thermal Effects on the Surface Plasmon Resonance of Cu Nanoparticles in Phosphate Glass: Impact on Cu^+ Luminescence. *Nanoscale Adv.* **2019**, *1*, 1826–1832. [CrossRef]
40. Sundari, S.T.; Chandra, S.; Tyagi, A.K. Temperature Dependent Optical Properties of Silver from Spectroscopic Ellipsometry and Density Functional Theory Calculations. *J. Appl. Phys.* **2013**, *114*, 033515. [CrossRef]
41. Tripura Sundari, S.; Srinivasu, K.; Dash, S.; Tyagi, A.K. Temperature Evolution of Optical Constants and Their Tuning in Silver. *Solid State Commun.* **2013**, *167*, 36–39. [CrossRef]
42. Brandt, T.; Hövel, M.; Gompf, B.; Dressel, M. Temperature- and Frequency-Dependent Optical Properties of Ultrathin Au Films. *Phys. Rev. B* **2008**, *78*, 205409. [CrossRef]
43. Reddy, H.; Guler, U.; Kildishev, A.V.; Boltasseva, A.; Shalaev, V.M. Temperature-Dependent Optical Properties of Gold Thin Films. *Opt. Mater. Express* **2016**, *6*, 2776. [CrossRef]
44. Shen, P.-T.; Sivan, Y.; Lin, C.-W.; Liu, H.-L.; Chang, C.-W.; Chu, S.-W. Temperature- and Roughness-Dependent Permittivity of Annealed/Unannealed Gold Films. *Opt. Express* **2016**, *24*, 19254. [CrossRef]
45. Jayanti, S.V.; Park, J.H.; Dejneka, A.; Chvostova, D.; McPeak, K.M.; Chen, X.; Oh, S.-H.; Norris, D.J. Low-Temperature Enhancement of Plasmonic Performance in Silver Films. *Opt. Mater. Express* **2015**, *5*, 1147. [CrossRef]

46. Dalacu, D.; Martinu, L. Temperature Dependence of the Surface Plasmon Resonance of Au/SiO2 Nanocomposite Films. *Appl. Phys. Lett.* **2000**, *77*, 4283–4285. [CrossRef]
47. Daneshfar, N. Temperature Dependence of the Optical Characteristics and Surface Plasmon Resonance of Core-Shell Nanoparticles. *Phys. Plasmas* **2014**, *21*, 063301. [CrossRef]
48. Bouillard, J.-S.G.; Dickson, W.; O'Connor, D.P.; Wurtz, G.A.; Zayats, A.V. Low-Temperature Plasmonics of Metallic Nanostructures. *Nano Lett.* **2012**, *12*, 1561–1565. [CrossRef]
49. Reddy, H.; Guler, U.; Kudyshev, Z.; Kildishev, A.V.; Shalaev, V.M.; Boltasseva, A. Temperature-Dependent Optical Properties of Plasmonic Titanium Nitride Thin Films. *ACS Photonics* **2017**, *4*, 1413–1420. [CrossRef]
50. Kreibig, U.; Vollmer, M. *Optical Properties of Metal Clusters*; Springer Series in Materials Science; Springer: Berlin/Heidelberg, Germany, 1995; Volume 25, ISBN 978-3-642-08191-0.
51. Kreibig, U. Electronic Properties of Small Silver Particles: The Optical Constants and Their Temperature Dependence. *J. Phys. F Met. Phys.* **1974**, *4*, 999–1014. [CrossRef]
52. Doremus, R.H. Optical Properties of Small Gold Particles. *J. Chem. Phys.* **1964**, *40*, 2389–2396. [CrossRef]
53. Doremus, R.H. Optical Properties of Small Silver Particles. *J. Chem. Phys.* **1965**, *42*, 414–417. [CrossRef]
54. Mulvaney, P. Metal Nanoparticles: Double Layers, Optical Properties, and Electrochemistry. In *Nanoscale Materials in Chemistry*; Klabunde, K.J., Ed.; Wiley: New York, NY, USA; Weinheim, Germany, 2001; ISBN 978-0-471-38395-6.
55. Tsarmpopoulou, M.; Ntemogiannis, D.; Stamatelatos, A.; Geralis, D.; Karoutsos, V.; Sigalas, M.; Poulopoulos, P.; Grammatikopoulos, S. Silver Nanoparticles' Localized Surface Plasmon Resonances Emerged at Polymeric Environments by Theory and Experiment. *Micro* **2024**, *4*, 318–333. [CrossRef]
56. Stamatelatos, A.; Tsarmpopoulou, M.; Geralis, D.; Chronis, A.G.; Karoutsos, V.; Ntemogiannis, D.; Maratos, D.M.; Grammatikopoulos, S.; Sigalas, M.; Poulopoulos, P. Interpretation of Localized Surface Plasmonic Resonances of Gold Nanoparticles Covered by Polymeric Coatings. *Photonics* **2023**, *10*, 408. [CrossRef]
57. Vitos, L.; Ruban, A.V.; Skriver, H.L.; Kollár, J. The Surface Energy of Metals. *Surf. Sci.* **1998**, *411*, 186–202. [CrossRef]
58. Wu, Y.-C.; Wang, L.-W.; Lai, C.-H. Low-Temperature Ordering of (001) Granular FePt Films by Inserting Ultrathin SiO_2 Layers. *Appl. Phys. Lett.* **2007**, *91*, 072502. [CrossRef]
59. Grammatikopoulos, S.; Pappas, S.; Dracopoulos, V.; Poulopoulos, P.; Fumagalli, P.; Velgakis, M.; Politis, C. Self-Assembled Au Nanoparticles on Heated Corning Glass by Dc Magnetron Sputtering: Size-Dependent Surface Plasmon Resonance Tuning. *J. Nanopart. Res.* **2013**, *15*, 1446. [CrossRef]
60. Ntemogiannis, D.; Tsarmpopoulou, M.; Stamatelatos, A.; Grammatikopoulos, S.; Karoutsos, V.; Anyfantis, D.I.; Barnasas, A.; Alexopoulos, V.; Giantzelidis, K.; Ndoj, E.A.; et al. ZnO Matrices as a Platform for Tunable Localized Surface Plasmon Resonances of Silver Nanoparticles. *Coatings* **2024**, *14*, 69. [CrossRef]
61. Karoutsos, V. Scanning Probe Microscopy: Instrumentation and Applications on Thin Films and Magnetic Multilayers. *J. Nanosci. Nanotechnol.* **2009**, *9*, 6783–6798. [CrossRef]
62. Solakidou, M.; Theodorakopoulos, M.; Deligiannakis, Y.; Louloudi, M. Double-Ligand Fe, Ru Catalysts: A Novel Route for Enhanced H2 Production from Formic Acid. *Int. J. Hydrogen Energy* **2020**, *45*, 17367–17377. [CrossRef]
63. Stamatelatos, A.; Tsarmpopoulou, M.; Chronis, A.G.; Kanistras, N.; Anyfantis, D.I.; Violatzi, E.; Geralis, D.; Sigalas, M.M.; Poulopoulos, P.; Grammatikopoulos, S. Optical Interpretation for Plasmonic Adjustment of Nanostructured Ag-NiO Thin Films. *Int. J. Mod. Phys. B* **2021**, *35*, 2150093. [CrossRef]
64. Chronis, A.G.; Stamatelatos, A.; Grammatikopoulos, S.; Sigalas, M.M.; Karoutsos, V.; Maratos, D.M.; Lysandrou, S.P.; Trachylis, D.; Politis, C.; Poulopoulos, P. Microstructure and Plasmonic Behavior of Self-Assembled Silver Nanoparticles and Nanorings. *J. Appl. Phys.* **2019**, *125*, 023106. [CrossRef]
65. Moharam, M.G.; Gaylord, T.K. Rigorous Coupled-Wave Analysis of Metallic Surface-Relief Gratings. *J. Opt. Soc. Am. A* **1986**, *3*, 1780. [CrossRef]
66. Scaffardi, L.B.; Pellegri, N.; de Sanctis, O.; Tocho, J.O. Sizing Gold Nanoparticles by Optical Extinction Spectroscopy. *Nanotechnology* **2005**, *16*, 158–163. [CrossRef]
67. Meier, M.; Wokaun, A. Enhanced Fields on Large Metal Particles: Dynamic Depolarization. *Opt. Lett.* **1983**, *8*, 581. [CrossRef] [PubMed]
68. Kuwata, H.; Tamaru, H.; Esumi, K.; Miyano, K. Resonant Light Scattering from Metal Nanoparticles: Practical Analysis beyond Rayleigh Approximation. *Appl. Phys. Lett.* **2003**, *83*, 4625–4627. [CrossRef]
69. Tsarmpopoulou, M.; Chronis, A.G.; Sigalas, M.; Stamatelatos, A.; Poulopoulos, P.; Grammatikopoulos, S. Calculation of the Localized Surface Plasmon Resonances of Au Nanoparticles Embedded in NiO. *Solids* **2022**, *3*, 55–65. [CrossRef]
70. Grammatikopoulos, S.; Stamatelatos, A.; Delimitis, A.; Sousanis, A.; Chrisanthopoulou, A.; Trachylis, D.; Politis, C.; Poulopoulos, P. Growth of Au Nanoparticles in NiO via Short Annealing of Precursor Material Thin Film and Optimization of Plasmonics. *Phys. Status Solidi A* **2017**, *214*, 1700303. [CrossRef]
71. Kasarova, S.N.; Sultanova, N.G.; Nikolov, I.D. Temperature Dependence of Refractive Characteristics of Optical Plastics. *J. Phys. Conf. Ser.* **2010**, *253*, 012028. [CrossRef]
72. Waxler, R.M.; Cleek, G.W. The Effect of Temperature and Pressure on the Refractive Index of Some Oxide Glasses. *J. Res. Natl. Bur. Stan. Sect. A* **1973**, *77*, 755. [CrossRef]

73. Jiménez Riobóo, R.J.; Philipp, M.; Ramos, M.A.; Krüger, J.K. Concentration and Temperature Dependence of the Refractive Index of Ethanol-Water Mixtures: Influence of Intermolecular Interactions. *Eur. Phys. J. E* **2009**, *30*, 19. [CrossRef]
74. Ben'kovskii, V.G.; Bogoslovskaya, T.M.; Nauruzov, M.K. Density, Surface Tension and Refractive Index of Aromatic Hydrocarbons at Low Temperatures. *Chem. Technol. Fuels Oils* **1966**, *2*, 23–26. [CrossRef]
75. Schulz, B.; Baberschke, K. Crossover from In-Plane to Perpendicular Magnetization in Ultrathin Ni/Cu(001) Films. *Phys. Rev. B* **1994**, *50*, 13467–13471. [CrossRef]

Disclaimer/Publisher's Note: The statements, opinions and data contained in all publications are solely those of the individual author(s) and contributor(s) and not of MDPI and/or the editor(s). MDPI and/or the editor(s) disclaim responsibility for any injury to people or property resulting from any ideas, methods, instructions or products referred to in the content.